

# Functionally Strain-Graded Nanoscoops for High Power Li-Ion Battery Anodes

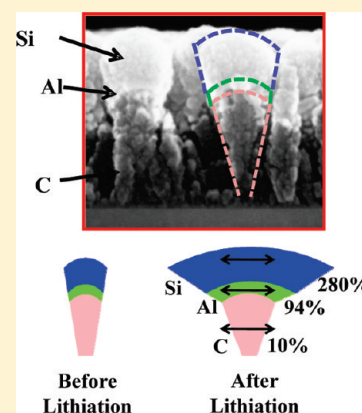
Rahul Krishnan,<sup>†</sup> Toh-Ming Lu,<sup>‡</sup> and Nikhil Koratkar<sup>\*,§</sup>

<sup>†</sup>Department of Materials Science and Engineering, <sup>‡</sup>Department of Physics, Applied Physics and Astronomy, and <sup>§</sup>Department of Mechanical, Aerospace and Nuclear Engineering, Rensselaer Polytechnic Institute, Troy, New York 12180, United States

**S** Supporting Information

**ABSTRACT:** Lithium-ion batteries show poor performance for high power applications involving ultrafast charging/discharging rates. Here we report a functionally strain-graded carbon–aluminum–silicon anode architecture that overcomes this drawback. It consists of an array of nanostructures each comprising an amorphous carbon nanorod with an intermediate layer of aluminum that is finally capped by a silicon nanoscoop on the very top. The gradation in strain arises from graded levels of volumetric expansion in these three materials on alloying with lithium. The introduction of aluminum as an intermediate layer enables the gradual transition of strain from carbon to silicon, thereby minimizing the mismatch at interfaces between differentially strained materials and enabling stable operation of the electrode under high-rate charge/discharge conditions. At an accelerated current density of  $\sim 51.2$  A/g (i.e., charge/discharge rate of  $\sim 40$ C), the strain-graded carbon–aluminum–silicon nanoscoop anode provides average capacities of  $\sim 412$  mAh/g with a power output of  $\sim 100$  kW/kg<sub>electrode</sub> continuously over 100 charge/discharge cycles.

**KEYWORDS:** Li-ion batteries, high power/rate capability, C–Al–Si nanoscoops, functionally strain graded materials



The rapid depletion of world oil reserves and their related hazards have propelled great advancements in hybrid and all-electric automobiles. Batteries designed for electric vehicles should be able to provide high energy and power densities. Lithium (Li)-ion batteries are known to deliver very high energy densities in comparison to other battery systems.<sup>1</sup> However, they suffer from low power densities. In contrast, supercapacitors provide very high power densities due to their surface-based reactions.<sup>2–4</sup> To replace a traditional combustion engine, it is highly desirable to combine the advantages of Li-ion batteries and supercapacitors into one single battery system. Earlier reports have shown the development of high rate cathode materials.<sup>5,6</sup> This has also led to an equal effort in the development of high-rate capable anode architectures. Silicon (Si) has been envisioned as a promising anode material because of its high theoretical capacity of  $\sim 4200$  mAh/g based on the stoichiometry of the alloy  $\text{Li}_{22}\text{Si}_5$ .<sup>7</sup> The main limitation of this high capacity is an accompanying volumetric expansion of  $\sim 400\%$  for crystalline Si (or  $\sim 280\%$  for amorphous Si) which results in pulverization and delamination of the electrode structure.<sup>8</sup> Pulverization results in more capacity losses due to increased solid electrolyte interphase (SEI) formation while delamination results in loss of electrical contact with the substrate. At higher charge/discharge rates (C-rates), these failure mechanisms are severely exacerbated and thus it is important to design architectures that perform well at fast C-rates to enable high power Li-ion rechargeable batteries.

One interesting approach to dealing with the stresses from Li–Si alloying has been the use of nanostructured Si instead of bulk Si. In addition to providing shorter Li-conduction distances, it is widely established that nanostructured Si has superior resistance to fracture because cracks do not reach their critical size for propagation.<sup>9</sup> Nanostructured Si also has reduced energy barriers for alloy formation, making it ideal for room temperature occurrence of Faradaic reactions.<sup>10</sup> A great step in this direction was taken by Cui and co-workers when they reported that Si nanowires provide nanoscale volume confinement which in turn prevents pulverization.<sup>11</sup> This was followed by several other architectures such as Si nanocolumns<sup>12</sup> and nanoparticles<sup>13,14</sup> which all performed well at low charge/discharge rates. For high rate anodes, there have been reports of composite structures which consist of active nano-Si in combination with a less active network structure. This enables faster electron conduction (via the network) along with high surface area of Si both of which result in better performance at high charge/discharge rates. Such work includes Si/TiSi<sub>2</sub> heteronanostructures<sup>15</sup> and dendritic carbon coated with Si nanoparticles.<sup>16</sup> Carbon-coated Si nanotubes have also been tested at rates as high as  $\sim 5$ C (15 A/g).<sup>17</sup> Note that very thin Si films ( $\sim 40$ – $50$  nm thick) show good cyclability at high C-rates ( $>12$ C).<sup>18–20</sup> However stress-induced

**Received:** August 23, 2010

**Revised:** December 21, 2010

**Published:** December 30, 2010

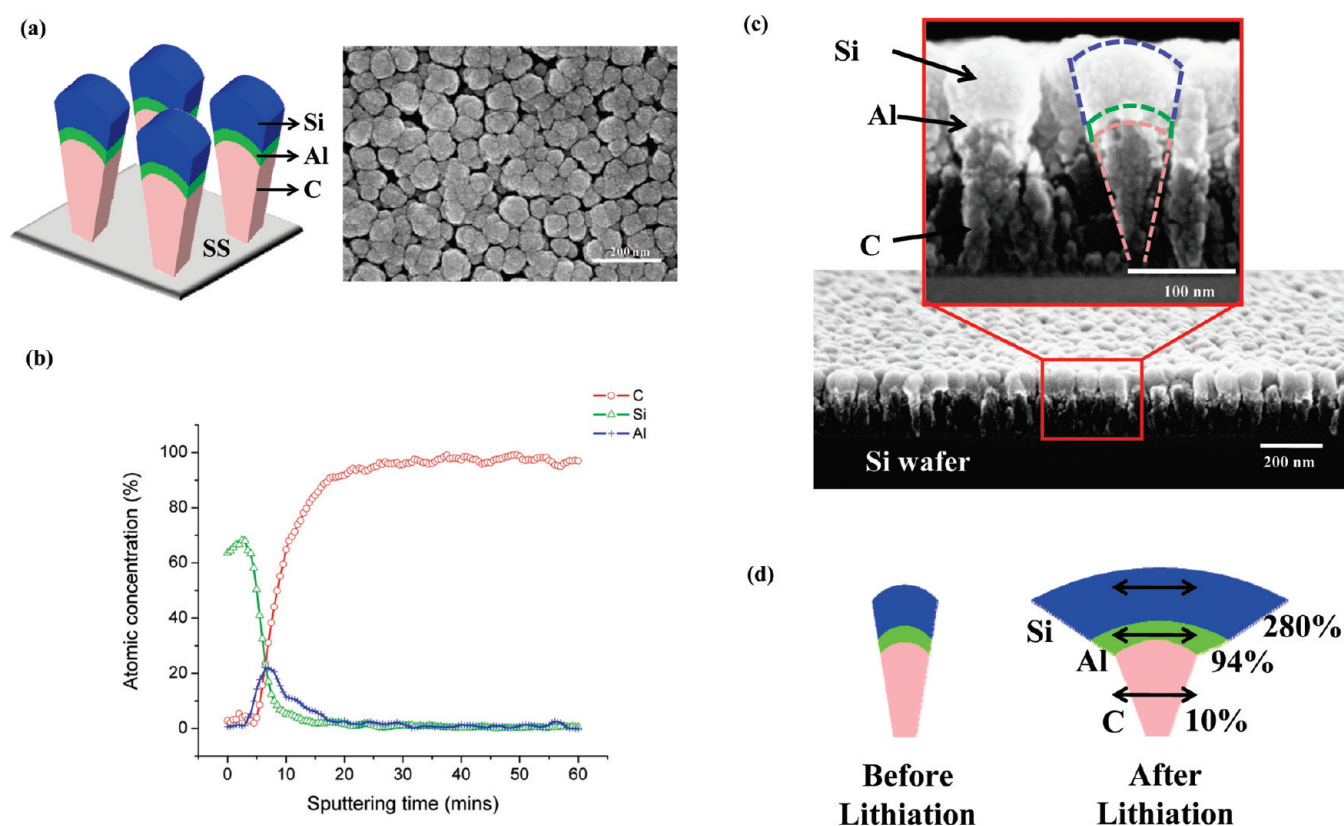


**Figure 1.** (a) The left schematic shows the C–Al–Si nanoscoop structure deposited on SS. The right scanning electron microscope (SEM) image shows the top view of the as-fabricated C–Al–Si nanoscoop structures on SS. (b) X-ray photoelectron spectroscopy (XPS) depth profile of the as-fabricated C–Al–Si nanoscoop structures on SS. (c) Cross-sectional SEM view of C–Al–Si nanoscoop structures deposited on a Si wafer. A magnified cross-section image is also shown with the C, Al, and Si regions demarcated. (d) Illustration of the principle of strain-graded multilayer nanostructures.

cracking in thicker films limits the scalability of such architectures. In a recent breakthrough, thicker films comprised of functionalized multiwalled carbon nanotubes deposited using a layer-by-layer self-assembly technique were found to deliver high power and energy densities.<sup>21</sup>

A review of the literature indicates that silicon–carbon composites<sup>22–28</sup> have often been studied as anode materials since carbon (C) forms a stable SEI<sup>29</sup> while Si provides enhanced capacity. However there is a vast difference in the volumetric strains developed in C (~10%) and Si (~280% for amorphous Si) due to their different Li uptake capacities.<sup>30</sup> The interface formed between materials that experience drastically different strain conditions is highly susceptible to fracture/delamination and is unable to accommodate the rapid volume changes that occur under high rate cycling conditions. By introducing materials between Si and C that have intermediate volumetric strains, a natural strain gradation can be developed in the multilayer architecture. Thus in the lithiated state, these intermediate materials would help to gradually transition the strain from the least strained material (like C) to the most strained material (like Si). Such a strain-graded nanoarchitecture could efficiently uptake lithium even under extremely rapid rates resulting in anodes that could potentially deliver high power and high energy density simultaneously.

Here we report the use of aluminum (Al) as an intermediate layer between C and Si to generate a functionally strain-graded nanoscoop architecture that can provide average capacities of ~412 mAh/g with a power output of ~100 kW/kg continuously over 100 cycles. Even when the power output is as high as ~250

kW/kg, the average capacity over 100 cycles is still ~90 mAh/g. In all gravimetric density calculations, the total mass of the electrode (including C, Al, and Si) has been considered. The architecture consists of an array of C nanorods (~170 nm long), each with an intermediate layer of Al (~13 nm thick) and finally capped by a scoop of Si (~40 nm thick). Stainless steel (SS) was used as the conducting substrate. Figure 1a (left) shows the sketch of the resulting C–Al–Si strain-graded anode architecture. The entire composite nanostructure array was deposited using dc magnetron sputtering with oblique or glancing angle deposition (OAD or GLAD) and required no patterning or lithography steps. This technique can efficiently generate an array of composite nanoscoops on a large area in an inexpensive manner. Besides, the ability to make the trimaterial composite with a nanorod base gives better 1-D electron conductivity to the stainless steel substrate. Inclination of the substrate to an angle of ~85° (measured from the substrate normal) with respect to the deposition source and substrate rotation (speed of ~30 rpm) result in a shadowing phenomenon<sup>31,12</sup> which yields well-separated amorphous C nanorods. Al and Si were then deposited in succession with flux incidence normal to the C nanorods. The experimental setup for the deposition of all three materials is illustrated in Figure S1 (Supporting Information). Figure 1a (right) shows the top view scanning electron microscope (SEM) image of the multilayer nanoscoops as deposited on stainless steel. Silicon wafer was used as the substrate for the cross-section images in Figure 1c since it is easy to cleave. However, the morphology remains the same even on stainless steel as the deposition technique yields the same structure independent of

the type of substrate used. This is justified by the fact that the top-view SEM image of the C–Al–Si nanoscoops on stainless steel (shown in Figure 1a) looks identical to those on Si wafer (Supplementary Figure S2, Supporting Information). The as-deposited C–Al–Si nanoscoop structure on stainless steel was analyzed for depth profile with X-ray photoelectron spectroscopy (XPS). Typical results are shown in Figure 1b; the peak positions of the three elements in the depth profile were displaced clearly in the order of Si, Al, and C from the sample surface down the depth. This profile is in agreement with the structure of the composite nanoscoops. The XPS scans (not shown here) also confirmed the presence of surface oxide in Si and Al with the majority being elemental Si, Al, and C. X-ray diffraction (XRD) pattern from the as-deposited C–Al–Si sample shows the presence of amorphous C and Si along with polycrystalline Al and lower intensity Fe peaks originating from the stainless steel (Figure S3, Supporting Information).

The choice of Al as the intermediate layer in the strain-graded composite is justified by the fact that in the lithiated condition it undergoes  $\sim 94\%$  volumetric expansion based on the stoichiometry of the alloy  $\text{LiAl}$ .<sup>30</sup> Thus the strain in Al is intermediate between that in C and Si. Besides it is an inexpensive metal and can be easily deposited by physical vapor deposition techniques. Al was initially proposed as the insertion anode material<sup>32</sup> as soon as the Li dendrite problem was identified in Li-ion batteries.<sup>33</sup> However large volumetric strains resulted in rapid capacity loss and thus Al was not a preferred insertion material. In fact recent reports show that even nanostructured Al has a rapid capacity loss<sup>34</sup> at low rates of 0.5C. Thus a thin layer of Al was chosen, enough to just provide a strain gradient from carbon to silicon in the lithiated state. C and Si deposited by dc magnetron sputtering were amorphous in nature consistent with earlier reports.<sup>35,36</sup> Our concept of strain gradation is elucidated in Figure 1d. In a theoretically lithiated state, C, Al, and Si would expand by  $\sim 10\%$ ,  $\sim 94\%$ , and  $\sim 280\%$ , respectively. Such a strain gradation from C toward Si would provide for a less abrupt transition across the material interfaces. Besides, the C nanorod tips offer nanostructured wavy interfaces. As a result the Si and the Al layers can relax their built-up strain by undergoing out-of-plane displacements as opposed to a flat interface where strain relaxation can occur only by delamination.<sup>37,38</sup> All of the above factors contribute to highly stress resistant interfaces between the C, Al, and Si in our nanoscoop architecture.

The C–Al–Si graded nanoscoop electrode was assembled against Li metal in a two-electrode coin cell (2032). All assembled cells were run through one cycle of cyclic voltammetry (CV) from 0.05 to 1.5 V at a scan rate of 10 mV/s to ensure that the cell does not exhibit a resistive behavior (Figure S4, Supporting Information). Figure 2a shows the charge/discharge voltage profiles between 0.05 and 2 V at current densities of  $\sim 1.28$  A/g (1C),  $\sim 12.8$  A/g (10C),  $\sim 51.2$  A/g (40C),  $\sim 76.8$  A/g (60C), and  $\sim 128$  A/g (100C). At a low C-rate such as  $\sim 1.28$  A/g, the electrode achieves a first discharge capacity as high as  $\sim 1230.9$  mAh/g with a Coulombic efficiency of  $\sim 96.4\%$ . This is very close to the theoretical capacity of  $\sim 1280$  mAh/g obtained from a weighted average of the theoretical capacities of carbon (372 mAh/g based on  $\text{LiC}_6$ ), aluminum (993 mAh/g based on  $\text{LiAl}$ ), and silicon (4200 mAh/g based on  $\text{Li}_{22}\text{Si}_5$ ). The voltage profile at 128 A/g (100C) shows a capacitance behavior and thus it is the limit of the operating rates. It is unlikely that even partial insertion of  $\text{Li}^+$  occurs at C-rates of the order of 100C. However, at rates as high as  $\sim 51.2$  A/g (40C), partial insertion and removal of  $\text{Li}^+$  occurs as can be seen from the

plateau in the voltage profile. At rates of  $\sim 51.2$ ,  $\sim 76.8$ , and  $\sim 128$  A/g, the first discharge capacities achieved were  $\sim 428.93$ ,  $\sim 343.98$ , and  $\sim 185.28$  mAh/g with Coulombic efficiencies of  $\sim 98.8\%$ ,  $\sim 99.3\%$ , and  $\sim 98.9\%$  respectively. At various cycling rates, the overall Coulombic efficiency for the C–Al–Si strain-graded nanoscoop structure is very high. This could be due to a very stable SEI that does not breakdown even after several cycles. A large portion of the surface area of the composite nanorod is C which provides a stable SEI. The Al layer being sandwiched between Si and C is protected from SEI formation. It is very interesting to note that the top Si scoop is unprotected and yet the overall Coulombic efficiency is high. This suggests that the strain-graded structure mitigates fracture in the Si scoops thereby preventing formation of new SEI. It should be noted that a volume expansion of 280% for the amorphous Si nanoscoop corresponds to a linear expansion of only  $\sim 56\%$  (in one dimension). Moreover, the absolute value of the expansion in radius is smaller than the expansion in height given the aspect ratio of these structures. Thus the spacing between the nanostructures (Figure 1a) is acceptable since the majority of the increase in linear dimension will be seen in the height. This is consistent with the cross-section SEM images of the lithiated nanostructures (both high rate and low rate) shown later in Figure 4.

Figure 2b shows the differential capacity curve as a function of voltage for the first and 10th cycles. The C-rate here was  $\sim 1\text{C}$  which is in the same range as that used by other groups.<sup>24</sup> While the system is not under thermodynamic equilibrium at 1C, this C-rate is low enough to ensure that the information derived from the data is meaningful. In the first cycle, the discharge differential capacity curve shows three main peaks at  $\sim 0.23$ ,  $\sim 0.14$ , and  $\sim 0.06$  V. The peak at 0.23 V could be attributed to the formation of an amorphous  $\text{Li}_x\text{Si}$  phase.<sup>39</sup> The peak at 0.14 V could correspond to Li intercalation in Al.<sup>40</sup> The peak at 60 mV is reported to correspond to the transformation of amorphous  $\text{Li}_x\text{Si}$  to a rapid crystallization of  $\text{Li}_{15}\text{Si}_4$ .<sup>39</sup> During the charge cycle, there are two peaks at 0.3 and 0.48 V which could potentially correspond to delithiation into amorphous  $\text{Li}_x\text{Si}$  phases.<sup>39</sup> For the 10th discharge cycle, the peak at 0.14 V seems to disappear. This could indicate a potential shift in the Al lithiation mechanism. The charge cycle also shows a small peak between 0.1 and 0.2 V. This could be related to the carbon dealloying reaction as is normally seen in the CV of natural graphite.<sup>41</sup> For the lithiation case, the peaks of C appear to be shadowed by the Si lithiation peaks.

Figure 2c shows the performance of the C–Al–Si electrode against Li metal over 100 cycles at constant current densities of  $\sim 51.2$  A/g (40C),  $\sim 76.8$  A/g (60C), and  $\sim 128$  A/g (100C). Note that in all our energy and power density calculations, the total mass of the electrode (including C, Al and Si) has been considered. The potential window used for these constant current charge/discharge tests was 0.05–2 V. These C-rates were calculated based on the theoretical capacity of the composite as indicated earlier, i.e.,  $1\text{C} = 1.28$  A/g. Even at a very high C-rate of 40C (i.e., current density of  $\sim 51.2$  A/g), the average capacity obtained over 100 cycles for the C–Al–Si system is  $\sim 412$  mAh/g with a capacity fade of only  $\sim 0.2\%$  per cycle. When the current density is increased to  $\sim 76.8$  A/g (i.e., C-rate of 60C), the average capacity over 100 cycles is  $\sim 330$  mAh/g with a capacity retention of  $\sim 90\%$  after 100 cycles. In comparison to the previous case, this C-rate is about 1.5 times higher and yet the average specific capacity over 100 cycles is 80% of that obtained at  $\sim 51.2$  A/g. The high capacity retention after 100 cycles could



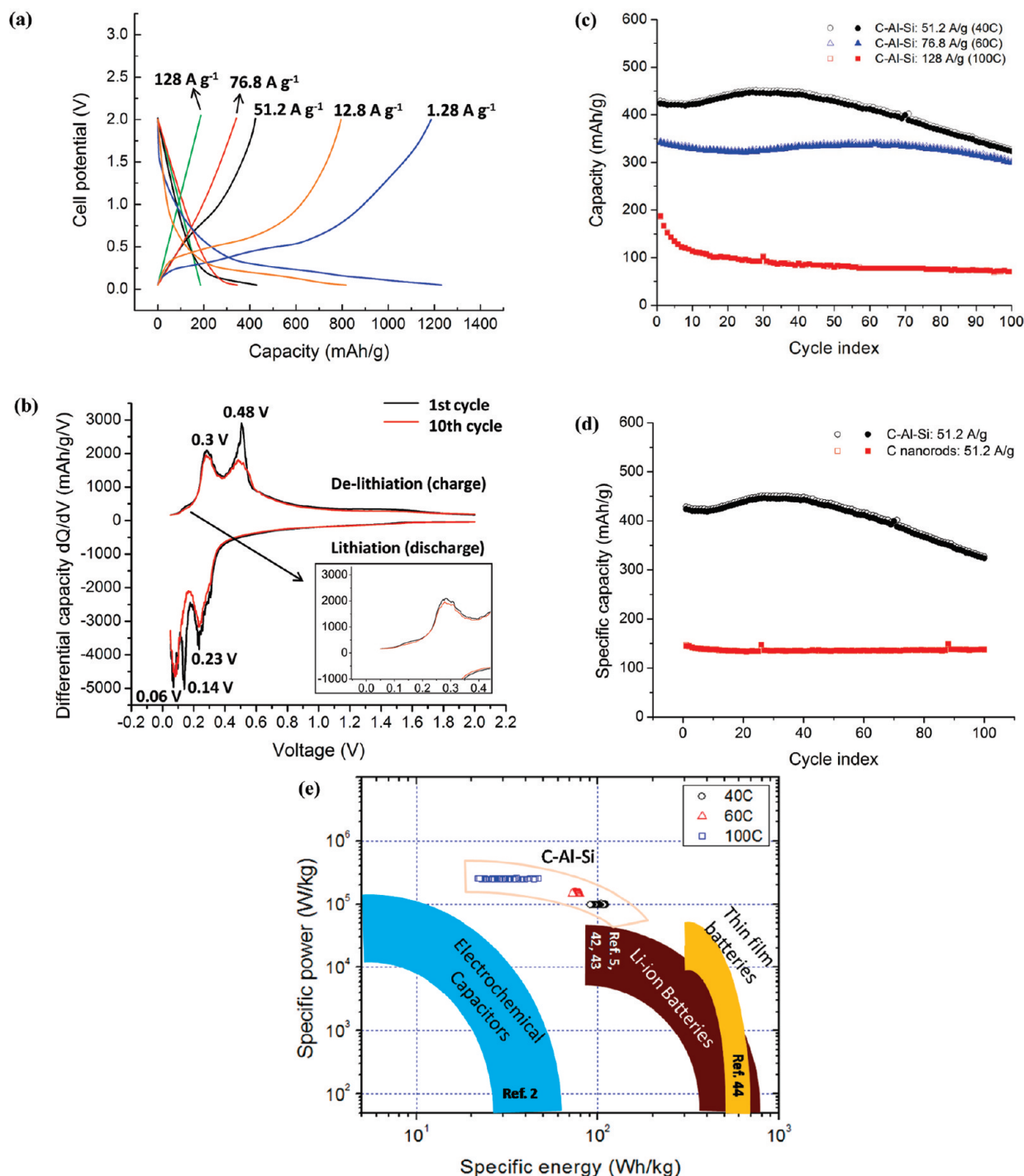


**Figure 2.** (a) First charge/discharge voltage profiles obtained from the C-Al-Si electrodes at rates varying from  $\sim 1.28$  A/g (1C) to  $\sim 128$  A/g (100C). (b) Differential capacity curve for C-Al-Si electrodes at 1C plotted for the first and the 10th cycles. Also shown in the inset is a magnified version of the delithiation peak between 0.1 and 0.2 V. (c) Capacity as a function of cycle index shown for C-Al-Si electrodes at  $\sim 51.2$ ,  $\sim 76.8$ , and  $\sim 128$  A/g over 100 cycles. The empty symbols represent discharge capacity while the filled symbols represent charge capacity in each case. (d) Comparison at  $\sim 51.2$  A/g current density of the charge/discharge capacity versus cycle number for the C-Al-Si electrode versus an electrode comprised of only C nanorods. The length and diameter of the C nanorods in the control sample are identical to those of the C nanorods in the C-Al-Si multilayer structure. (e) Ragone plot showing C-Al-Si electrode performance at all the above three rates for the entire 100 cycles. Also shown are the regions on the Ragone plot occupied by electrochemical capacitors,<sup>2,21</sup> Li-ion batteries<sup>5,42,43</sup> and thin film batteries.<sup>44</sup> In all gravimetric density calculations, only the active electrode mass (including C, Al, and Si) has been considered. Similarly the data taken from refs 5 and 42–44 for Li-ion batteries and thin film batteries are based on the active electrode mass only. The data for electrochemical capacitors (ref 2) was extrapolated considering only the active electrode mass based on the analysis shown in ref<sup>21</sup>.

be attributed to the stable SEI and efficient volume change due to the stain-graded multilayer architecture. At an accelerated cur-

rent density of  $\sim 128$  A/g (C-rate of 100C), the average capacity over 100 cycles is  $\sim 90$  mAh/g. In this case there is a  $\sim 36\%$

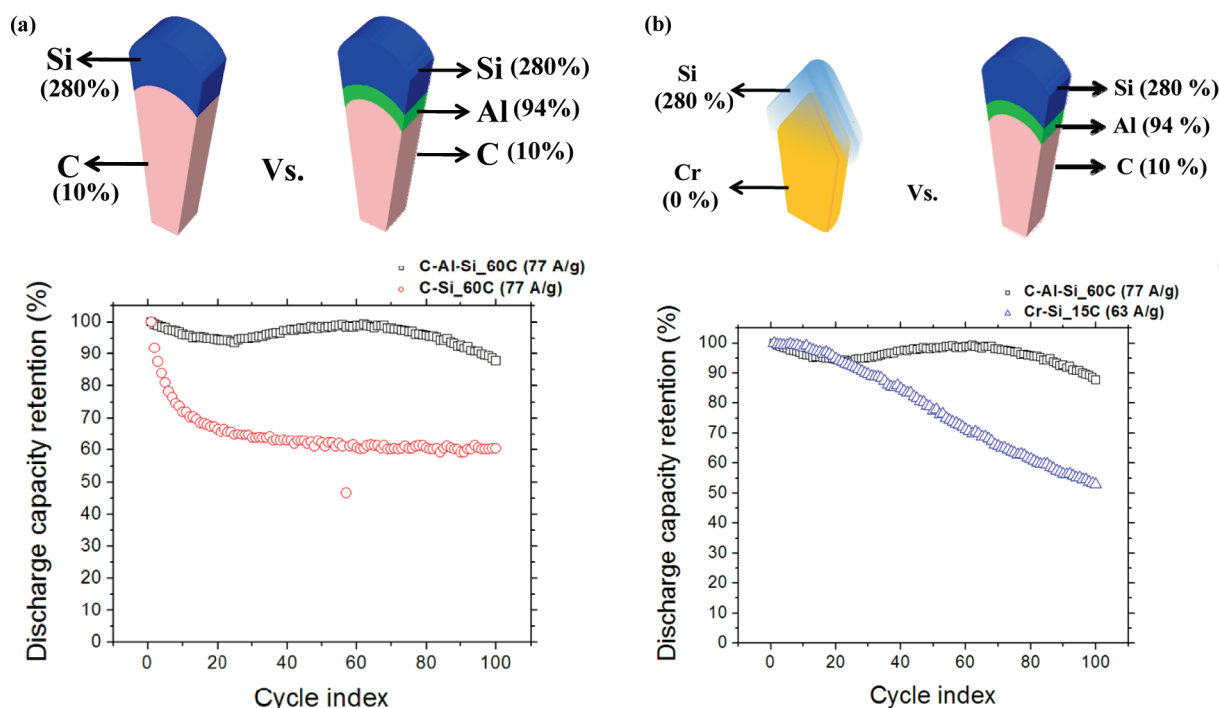


**Figure 3.** (a) Discharge capacity retention over 100 cycles for the C–Al–Si architecture as compared with the C–Si system. Inclusion of Al as an intermediate layer between C and Si improves the capacity retention from  $\sim 60\%$  to  $\sim 90\%$  at the end of 100 cycles. The C-rate used for both the systems was  $\sim 60C$ . (b) Comparison of discharge capacity retention between C–Al–Si system (current density of  $\sim 77$  A/g) and a Si nanoscoop on a Cr nanorod operated at  $\sim 63$  A/g. Since Cr does not alloy with Li, there is no volume expansion in Cr resulting in no strain gradation. There is a constant degradation in the capacity all the way to  $\sim 50\%$  by the 100th cycle in the case of no strain gradation. These two cases illustrate how the capacity degradation can be greatly reduced by using a C–Al–Si strain-graded architecture.

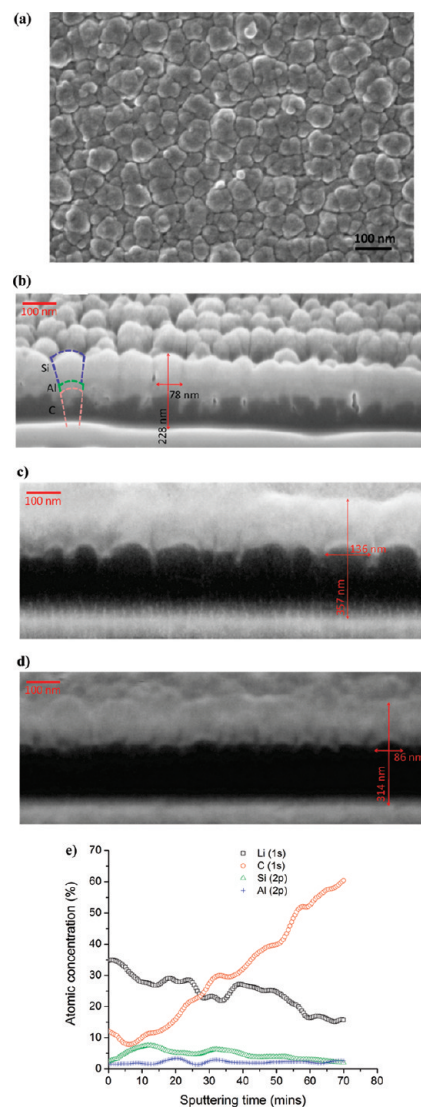
capacity drop within the first 10 cycles after which the capacity fade stabilizes to about  $\sim 0.35\%$  per cycle. However it should be noted that at 128 A/g, the power density for the C–Al–Si system (based on the electrode weight) is exceptionally high ( $\sim 250$  kW/kg). To evaluate the performance of the C–Al–Si system, we also tested  $\sim 170$  nm long C nanorods as a control. Note that the length and diameter of the C nanorods in the control sample are identical to that of the C nanorods in the C–Al–Si multilayer nanostructures. The only difference being that we do not deposit Al and Si on the C nanorods. The charge/discharge capacities of the C nanorods were compared to the C–Al–Si nanostructures at an accelerated current density of  $\sim 51.2$  A/g (Figure 2d). The average capacity of the C nanorods was  $\sim 140$  mAh/g; note that the ideal capacity of  $\sim 372$  mAh/g for C is practically observed only at low charge/discharge rates. At ultrahigh rates, only partial lithiation occurs even for carbon, which explains the reduced capacity. However carbon offers excellent stability with cycle number as is evident from Figure 2d. The C–Al–Si nanostructures show an average capacity of  $\sim 412$  mAh/g which is  $\sim 3$ -fold better than C alone. This indicates that Si is indeed being partially lithiated and this plays a vital role in boosting the overall charge capacity at ultrafast rates. Moreover the capacity retention over 100 cycles that we show (Figure 2c,d) is unprecedented for any Si based electrode cycled at such ultrahigh charge/discharge rates.

Figure 2e shows a “Ragone plot” with data from the C–Al–Si electrodes under the three different cycling rates. It is to be noted that for each current density, data from all 100 cycles have been depicted on the Ragone plot. At lower rates such as 40C and 60C, the power density and energy density remain nearly constant through all 100 cycles. Overall, it is clear that the C–Al–Si

strain-graded anode architecture simultaneously achieves energy densities of over 100 W h/kg<sub>electrode</sub> and power densities of over 100 kW/kg<sub>electrode</sub>. Importantly, these levels of power and energy density not only are achieved merely for a few initial cycles but also are maintained over a hundred continuous charge/discharge cycles. Note that the total mass of the nanostructures (including C, Al, and Si) has been considered in the energy and power density calculations. In the plot we also compare the performance of the C–Al–Si anode to the published literature<sup>2,5,21,42–44</sup> for electrochemical capacitors, Li-ion batteries, and thin film batteries. Only the active electrode mass was considered in these studies thereby making this a valid comparison with the C–Al–Si electrode. It is clear from the plot that the C–Al–Si electrodes provide the optimum combination of both high power density and high energy density.

The significance of the intermediate Al layer is illustrated by comparing the discharge capacity retention in the C–Al–Si system with a C–Si system (Figure 3a). The C–Si system consists of 170 nm long C nanorods with just a 40 nm thick Si nanoscoop and no intermediate Al layer. It can be seen that at the same C-rate of 60C, at the end of 100 cycles, there is  $\sim 90\%$  capacity retention in the C–Al–Si system while just  $\sim 60\%$  capacity retention in the C–Si system. This shows that including Al as an intermediate layer between C and Si significantly improves the capacity retention. We also tested (Figure 3b)  $\sim 40$  nm thick Si scoops deposited on 170 nm long chromium (Cr) nanorods. Note that the Cr nanorods do not alloy with Li and so there is no strain gradation at the Si–Cr interface. For this case also, the capacity loss is severe ( $\sim 50\%$  after 100 cycles) in comparison to the strain-graded C–Al–Si architecture.

The C–Al–Si electrode cycled at a rate of  $\sim 51.2$  A/g (40C) was characterized after 30 cycles using scanning electron microscopy (SEM) and X-ray photoelectron spectroscopy (XPS) with depth profile. The electrode was cycled until the 30th discharge cycle so that the salvaged electrode would be in the lithiated state. We believe that the increase in capacity during the first  $\sim 30$  cycles (Figure 2c) can be explained by a gradual increase in the uptake of  $\text{Li}^+$  during the initial cycles. This may occur due to the fact that the rate of charge/discharge is too fast to allow for full lithiation in the first cycle. In order to support this argument, we performed cross-section SEM analysis on the sample cycled to the 30th discharge cycle to detect for any apparent volumetric increase. Figure 4a shows the top view SEM image of the C–Al–Si composite nanoscoops on the stainless steel substrate after high rate cycling at  $\sim 51.2$  A/g (40C) until the 30th discharge cycle. In this image, the composite nanoscoops seem to be in an expanded state; this is confirmed by the loss of spacing between the nanostructures in this state. In order to get a clearer perspective of the volumetric change in these nanostructures, we attempted to get cross-section SEM images on stainless steel. A low current  $\text{Ga}^+$  focused ion beam (FIB) was used to mill through the film and create a cross-section cut (Supporting Information). A low current was used to obtain a clean cut surface with no redeposition. This cut face was then viewed using in situ SEM to get the cross-section images. Panels b, c, and d of Figure 4 show the cross-section SEM images of as-deposited C–Al–Si, sample discharged to the first cycle at 1C ( $\sim 1.28$  A/g) and sample discharged to the 30th cycle at 40C ( $\sim 51.2$  A/g). All three FIB section images were taken under identical conditions of ion probe current, electron beam voltage, and magnification so as to yield a valid comparison. The as-deposited composite nanostructures roughly measure to be  $\sim 228$  nm in height and  $\sim 78$  nm in diameter. After the first discharge (Li insertion) at 1C, the nanostructures swell up to  $\sim 357$  nm in height and  $\sim 136$  nm in diameter. Approximating to a cylindrical geometry, this volume increase corresponds to  $\sim 376\%$ . Given that this discharge was performed at a slow rate of  $\sim 1.28$  A/g (1C), it is expected to see a drastic increase in volume. After the 30th discharge at 40C, the nanostructures measure to be  $\sim 314$  nm in height and  $\sim 86$  nm in diameter. On the basis of the same cylinder geometry approximation, this volume increase corresponds to  $\sim 67\%$ . It should be noted that the calculated percentages of volume increase are only approximate estimates since the C–Al–Si is not perfectly cylindrical in geometry; these estimates give a sense of comparison between the volume changes at low and high rates. The fact that the volume increase is lower at high rates is not surprising given that the capacity decreases at higher rates. However, it is interesting to note that even at rapid rates such as  $\sim 51.2$  A/g (40C), there exists charge storage in the bulk which results in a volume increase. From the cross-section SEM image for C–Al–Si at 40C (Figure 4d), we can see that the C nanorod (dark contrast region) measures  $\sim 180$  nm, while the Al and Si scoop together (light contrast region) measures  $\sim 135$  nm. The as-deposited C–Al–Si structure measures about 228 nm totally with C  $\sim 170$  nm, Al and Si together  $\sim 58$  nm. This shows that after lithiation at 40C, the C nanorod itself expands minimally while most of the expansion can be seen in the Al and Si region. Note that even though there is a large volume increase, the C–Al–Si electrode is only partially lithiated at 40C. If the electrode was lithiating fully, the measured capacity at 40C should have been  $\sim 1280$  and not  $\sim 412$  mAh/g (Figure 2d). Similarly the volume expansion that we physically



**Figure 4.** (a) Top view scanning electron microscope (SEM) image of C–Al–Si nanoscoop structures on stainless steel after cycling at a rate of  $\sim 51.2$  A/g (40C) up to the 30th discharge cycle. Cross-section SEM images for C–Al–Si nanoscoop structures on stainless steel under the following conditions: (b) as-deposited, (c) after the first discharge cycle at a rate of  $\sim 1.28$  A/g (1C), and (d) after the 30th discharge cycle at a rate of  $\sim 51.2$  A/g (40C). (e) X-ray photoelectron spectroscopy (XPS) depth profile after cycling the C–Al–Si nanostructures at a rate of  $\sim 51.2$  A/g (40C) up to the 30th discharge cycle showing the relative atomic concentrations of Li, C, Al, and Si as a function of sputtering time.

measure from our cross-sectional SEM imaging is  $\sim 67\%$  at 40C as opposed to  $\sim 376\%$  at 1C. However because the capacity of Si is so high, even partial lithiation of Si has a dramatic impact on the capacity performance (Figure 2d) when compared with the control sample (C nanorod electrode). This is the reason why the C–Al–Si electrode can generate high energy density and high power density simultaneously.

We also observe that the expanded structure in the low rate case (Figure 4c) maintains the same aspect ratio as the as-deposited nanostructure while the expanded structure in the high rate case (Figure 4d) shows a higher aspect ratio. We believe that this difference in isotropic (low rate) versus anisotropic (high



rate) volume change indicates key differences in the  $\text{Li}^+$  flux in different directions. In the high rate case, there is probably a higher  $\text{Li}^+$  flux in the vertical direction than the lateral direction due to presence of a high local electric field. A similar cross-section image was taken from a C–Al–Si sample discharged to the first cycle at 40C (supplementary Figure S6a, Supporting Information). The volume increase was much lower for this case. Thus it is clear that it takes several cycles to see large volume changes in the structure. This means that within the first  $\sim 30$  cycles, the capacity keeps increasing due to more bulk inclusion of Li. This gradual increase in the Li uptake within the first  $\sim 30$  cycles could be responsible for the observed increase in specific capacity with cycle number (Figure 2c).

Figure 4e shows the XPS depth profile after cycling the C–Al–Si nanostructures at a rate of  $\sim 51.2$  A/g (40C) up to the 30th discharge cycle. XPS was alternated with  $\text{Ar}^+$  sputtering cycles each lasting 30 s. The sputter rate could not be calibrated to obtain the depth since the composite nanorods consisted of three materials with different sputtering rates. This is the reason why we report data only in terms of sputtering time and not in terms of depth. However, the XPS depth profile (Figure 4e) shows clear peaks for the three different regions (Si, Al, and C) as a function of sputter time. Overall, the first  $\sim 25$ – $30$  min of sputtering showed a major presence of  $\text{LiF}$  and  $\text{Li}_2\text{CO}_3$  with a minor presence of poly(ethylene oxide) (PEO)-type oligomers with the structure of  $-(\text{CH}_2\text{CH}_2\text{O})_n-$  and alkyl fluorocarbons all of which form the composition of the solid electrolyte interphase (SEI). These SEI compounds were identified from high-resolution scans of C (1s), O (1s), F (1s), and Li (1s). The scans are shown in Supplementary Figure S5 in the Supporting Information. The peak assignments (Supplementary Table S1, Supporting Information) were made based on published literature<sup>45–47</sup> and the online NIST XPS database.<sup>48</sup> The SEI composition reported here is in agreement with the XPS analysis of SEI on silicon nanowires reported earlier.<sup>49</sup> The Li (1s) signal shows a peak at  $\sim 57.25$  eV beyond  $\sim 23$  min of sputter time, which could possibly pertain to  $\text{LiC}_6$  based on the binding energy of 57.1 eV obtained from the NIST database.<sup>48</sup> Other alloy states such as Li–Si or Li–Al would be difficult to identify due to the lack of information on their binding energies. The C curve on the XPS depth profile shows an increasing atomic concentration with sputtering time as the base of the composite nanostructure is carbon which is attached to the stainless steel substrate. Si and Al curves show their presence somewhere between 10 and 20 min of sputtering time. This is in agreement with the position of Si and Al on the top of the C nanorod. Importantly the Li curve shows an overall decreasing trend starting from the Si, Al, and finally into the C regions. If the Li was being inserted into C and not Si, then there would be Li due to SEI only in Si and Li due to SEI plus alloying in the C region. Thus one would expect a clear increasing trend of Li concentration with depth as one moves from the Si into the carbon region. However, we see the opposite trend, with the Li concentration decreasing markedly as we transition from the Si into the Al and C regions. This means we now have a case of SEI plus alloy in both Si and C and since the capacity of Si is higher than C, the overall Li concentration is observed to be higher in Si than in C. This is also consistent with the cross-sectional SEM results for volume expansion shown previously in Figure 4b–d.

In summary, we report a novel functionally strain-graded C–Al–Si nanoscoop anode architecture that can achieve average capacities of  $\sim 412$  mAh/g with a power density of  $\sim 100$

kW/kg<sub>electrode</sub> (current density of  $\sim 51.2$  A/g) continuously through 100 cycles. We also show that the C–Al–Si composite can yield power densities as high as  $\sim 250$  kW/kg<sub>electrode</sub> (current density of  $\sim 128$  A/g) continuously over 100 cycles with an average capacity of  $\sim 90$  mAh/g. The C–Al–Si architecture has the potential for mass scalability by increased deposition time as well as the possibility of stacking C–Al–Si nanostructure films on intermediate carbon thin film supports. When the mechanism of charge generation involves alloying with the host material and the demand for current is high, the electrode architecture is put through large strain rates accompanied by rapid volume changes. In such a situation, a functionally strain-graded structure could potentially undergo rapid volume changes with reduced possibility of interfacial cracking or delamination. By building a strain-graded structure, it is possible to eliminate interfaces between materials that have a large strain difference during lithiation. Low strain difference between adjacent materials in the composite leads to highly efficient alloy–dealloy reactions preserving the overall structural integrity of the electrode. To further improve the strain gradient, we could potentially insert materials such as Sb (strain of  $\sim 147\%$ ) or As (strain of  $\sim 201\%$ ) between Al and Si. This will also help in increasing the area mass density while still improving the performance. Such strain-graded multilayer anode architectures show significant potential for the design of high power and high capacity Li-ion rechargeable batteries.

## ■ ASSOCIATED CONTENT

**S Supporting Information.** Experimental methods used for C–Al–Si electrode preparation, coin cell preparation, electrode testing, X-ray photoelectron spectroscopy (XPS), X-ray diffraction (XRD), focused ion beam (FIB) milling, and in situ SEM cross-sectional analysis of C–Al–Si electrodes, details of oblique angle deposition setup, cyclic voltammetry of electrode structures, and XPS data on the cycled samples, and the specific capacity vs cycle number for the C–Al–Si electrode at low charge/discharge rates ( $\sim 1\text{C}$ ). This material is available free of charge via the Internet at <http://pubs.acs.org>.

## ■ AUTHOR INFORMATION

### Corresponding Author

\*E-mail: [koratn@rpi.edu](mailto:koratn@rpi.edu).

## ■ ACKNOWLEDGMENT

N.K. and T.M.L. acknowledge funding support from the USA National Science Foundation (Award 0969895, with Dr. Dennis R. Carter serving as the program monitor) and the New York State's Energy Research and Development Authority (NYSERDA Award 18510, with Dr. Jennifer L. Harvey serving as program monitor). We thank the Center for Future Energy Systems at RPI for providing access to their battery test facility. We thank Dr. B. Tanto for valuable discussions and R. Planty's guidance in collecting XPS data. We also acknowledge the efforts of David Frey in making focused ion beam cuts for cross-sectional SEM analysis.

## ■ REFERENCES

- (1) Tarascon, J.-M.; Armand, M. *Nature* **2001**, *414*, 359–367.
- (2) Simon, P.; Gogotsi, Y. *Nat. Mater.* **2008**, *7*, 845–854.
- (3) Pushparaj, V. L.; Shaijumon, M. M.; Kumar, A.; Murugesan, S.; Ci, L.; Vajtai, R.; Linhardt, R. J.; Nalamasu, O.; Ajayan, P. M. *Proc. Natl. Acad. Sci. U.S.A.* **2007**, *104*, 13574.

- (4) Winter, M.; Brodd, R. J. *Chem. Rev.* **2004**, *104*, 4245–4269.
- (5) Kang, K.; Meng, Y. S.; Breger, J.; Grey, C. P.; Ceder, G. *Science* **2006**, *311*, 977–980.
- (6) Kang, B.; Ceder, G. *Nature* **2009**, *458*, 190–193.
- (7) Wang, W.; Datta, M. K.; Kumta, P. N. *J. Mater. Chem.* **2007**, *17*, 3229–3237.
- (8) Maranchi, J. P.; Hepps, A. F.; Evans, A. G.; Nuhfer, N. T.; Kumta, P. N. *J. Electrochem. Soc.* **2006**, *153*, A1246–A1253.
- (9) Graetz, J.; Ahn, C. C.; Yazami, R.; Fultz, B. *Electrochem. Solid State Lett.* **2003**, *6*, A194–A197.
- (10) Gao, B.; Sinha, S.; Fleming, L.; Zhou, O. *Adv. Mater.* **2001**, *13*, 816–819.
- (11) Chan, C. K.; Peng, H.; Lin, G.; McIlwrath, K.; Zhang, X. F.; Huggins, R. A.; Cui, Y. *Nat. Nanotechnol.* **2008**, *3*, 31–35.
- (12) Fleischauer, M. D.; Li, J.; Brett, M. J. *J. Electrochem. Soc.* **2009**, *156*, A33–A36.
- (13) Kwon, Y.; Park, G.-S.; Cho, J. *Electrochim. Acta* **2007**, *52*, 4663–4668.
- (14) Kim, H.; Seo, M.; Park, M.-H.; Cho, J. *Angew. Chem., Int. Ed.* **2010**, *49*, 2146–2149.
- (15) Zhao, S.; Liu, X.; Wang, D. *Nano Lett.* **2010**, *10*, 860–863.
- (16) Magasinski, A.; Dixon, P.; Hertzberg, B.; Kvit, A.; Ayala, J.; Yushin, G. *Nat. Mater.* **2010**, *9*, 353–358.
- (17) Park, M.-H.; Kim, M. G.; Joo, J.; Kim, K.; Kim, J.; Ahn, S.; Cui, Y.; Cho, J. *Nano Lett.* **2009**, *9*, 3844–3847.
- (18) Ohara, S.; Suzuki, J.; Sekine, K.; Takamura, T. *J. Power Sources* **2004**, *136*, 303–306.
- (19) Takamura, T.; Ohara, S.; Uehara, M.; Suzuki, J.; Sekine, K. *J. Power Sources* **2004**, *129*, 96–100.
- (20) Kasavajjula, U.; Wang, C.; Appleby, A. J. *J. Power Sources* **2007**, *163*, 1003–1039.
- (21) Lee, S. W.; Yabuuchi, N.; Gallant, B. M.; Chen, S.; Kim, B.-S.; Hammond, P. T.; Shao-Horn, Y. *Nat. Nanotechnol.* **2010**, *5*, 531–537.
- (22) Liu, W.-R.; Wang, J.-H.; Wu, H.-C.; Shieh, D.-T.; Yang, M.-H.; Wu, N.-L. *J. Electrochem. Soc.* **2005**, *152*, A1719.
- (23) Ng, S.-H.; Wang, J.; Wexler, D.; Konstantinov, K.; Guo, Z.-P.; Liu, H.-K. *Angew. Chem., Int. Ed.* **2006**, *45*, 6896.
- (24) Kim, H.; Cho, J. *Nano Lett.* **2008**, *8*, 3688.
- (25) Wang, W.; Kumta, P. N. *ACS Nano* **2010**, *4*, 2233–2241.
- (26) Cui, L.-F.; Yang, Y.; Hsu, C.-M.; Cui, Y. *Nano Lett.* **2009**, *9*, 3370–3374.
- (27) Chou, S.-L.; Wang, J.-Z.; Choucair, M.; Liu, H.-K.; Stride, J. A.; Dou, S.-X. *Electrochem. Commun.* **2010**, *12*, 303–306.
- (28) Chan, C. K.; Patel, R. N.; O'Connell, M. J.; Korgel, B. A.; Cui, Y. *ACS Nano* **2010**, *4*, 1443–1450.
- (29) Winter, M.; Appel, W. K.; Evers, B.; Hodal, T.; Moller, K.-C.; Schneider, I.; Wachtler, M.; Wagner, M. R.; Wrodnigg, G. H.; Besenhard, J. O. *Monatsh. Chem.* **2001**, *132*, 473–486.
- (30) Patil, A.; Patil, V.; Shin, D.; Choi, J.; Paik, D.; Yoon, S.-J. *Mater. Res. Bull.* **2008**, *43*, 1913–1942.
- (31) Karabacak, T.; Wang, G.-C.; Lu, T.-M. *J. Vac. Sci. Technol., A* **2004**, *22*, 1778–1784.
- (32) Baranski, A. S.; Fawcett, W. R. *J. Electrochem. Soc.* **1982**, *129*, 901–907.
- (33) Broussely, M.; Biensan, P.; Simon, B. *Electrochim. Acta* **1999**, *45*, 3–22.
- (34) Au, M.; McWhorter, S.; Ajo, H.; Adams, T.; Zhao, Y.; Gibbs, J. *J. Power Sources* **2010**, *195*, 3333–3337.
- (35) Subramanian, V.; Karabacak, T.; Masarapu, C.; Teki, R.; Lu, T.-M.; Wei, B. *J. Power Sources* **2010**, *195*, 2044–2049.
- (36) Karabacak, T.; Zhao, Y.-P.; Wang, G.-C.; Lu, T.-M. *Phys. Rev. B* **2001**, *64*, No. 085323.
- (37) Karabacak, T.; Picu, C. R.; Senkevich, J. J.; Wang, G.-C.; Lu, T.-M. *J. Appl. Phys.* **2004**, *96*, 5740–5746.
- (38) Teki, R.; Datta, M. K.; Krishnan, R.; Parker, T. C.; Lu, T.-M.; Kumta, P. N.; Koratkar, N. *Small* **2009**, *5*, 2236–2242.
- (39) Li, J.; Dahn, J. R. *J. Electrochem. Soc.* **2007**, *154*, A156–A161.
- (40) Hu, R.; Zeng, M.; Li, C. Y. V.; Zhu, M. *J. Power Sources* **2009**, *188*, 268–273.
- (41) Fujimoto, H. *J. Power Sources* **2010**, *195*, S019–S024.
- (42) Chen, H.; Armand, M.; Demailly, G.; Dolhem, F.; Poizot, P.; Tarascon, J.-M. *ChemSusChem* **2008**, *1*, 348–355.
- (43) Wu, X.-L.; Jiang, L.-Y.; Cao, F.-F.; Guo, Y.-G.; Wan, L.-J. *Adv. Mater.* **2009**, *21*, 2710–2714.
- (44) Dudney, J. N. *Electrochem. Soc. Interface* **2008**, *17*, 44–48.
- (45) Bryngelsson, H.; Stjern Dahl, M.; Gustafsson, T.; Edstrom, K. *J. Power Sources* **2007**, *174*, 970–975.
- (46) Edstrom, K.; Herstedt, M.; Abraham, D. P. *J. Power Sources* **2006**, *153*, 380–384.
- (47) Leroy, S.; Blanchard, F.; Dedryvere, R.; Martinez, H.; Carre, B.; Lemordant, D.; Gonbeau, D. *Surf. Interface Anal.* **2005**, *37*, 773–781.
- (48) NIST XPS database available online at <http://srdata.nist.gov/xps/Default.aspx> (Accessed on June 29, 2010).
- (49) Chan, C. K.; Ruffo, R.; Hong, S. S.; Cui, Y. *J. Power Sources* **2009**, *189*, 1132–1140.